QTAIM Analysis of Ligand Properties and Mechanisms of Tuning of 6-Membered Ring *N*-Heterocyclic Carbenes in Transition Metal Complexes through Ring-Substituent Variation

Lucius E. Johnson[†] and Donald B. DuPré*

Department of Chemistry, University of Louisville, Louisville, Kentucky 40292

Received: February 19, 2009; Revised Manuscript Received: May 4, 2009

Tuning of the ligand properties of a series of *N*-heterocyclic carbenes has previously been achieved through the variation of substituents at the ring boron sites. Analysis of the topology of the electron density using the quantum theory of atoms in molecules (QTAIM) reveals sensitive changes in the integrated atomic properties and the curvature of the valence shell charge concentration of the carbene carbon (C2). Amino substitution induces greater ligand-to-metal σ-donation in the transition metal complex, which in turn weakens the attractive potential energy density on the interatomic surface of the *trans*-carbonyl group leading to the decrease in the *trans* C−O stretching frequency observed experimentally and theoretically. The distribution of charge concentrations within the inner-valence shell of cobalt in the transition metal complexes recovers the QTAIM analogs of ligand-to-metal σ-donation and metal-to-ligand π-back-donation. Investigation of the virial of the Ehrenfest force acting on the interatomic surfaces shows the operative mechanism of ligand tuning to be the inductive withdrawal of charge from the ring by nitrogen and subsequent back-polarization of remaining charge toward C2. This mechanism is at odds with the orbital viewpoint of exo nitrogen-to-ring-boron π-back-donation; however, it is the electronic forces that govern the bonding and charge distribution within a molecule in a stationary state.

I. Introduction

N-Heterocyclic carbene−transition metal (NHC−TM) complexes have been used extensively in catalysis over the past four decades. In fact, Wanzlick and Öfele first reported TM complexes of singlet NHCs in 1968,[1] long before Arduengo first isolated a free NHC.[2] The strong nucleophilicity and increased stability of NHCs in TM complexes leads to increased catalytic activity over the long-used organophosphane ligands, PR_3.[3−6] Examples of their use in a variety of catalytic roles, including Heck and Suzuki coupling, olefin metathesis, and aryl amination, have been well documented.[3] Experimental studies of reactions of NHCs[5,7,8] and the decomposition of NHC−TM complexes have found their stability to vary. Chiral NHC−TM complexes have been developed for asymmetric catalysis,[9] and a free monoheteroatom (alkyl)(amino)carbene developed by Bertrand et al. has been recently shown to activate H_2 and NH_3.[10] As the scope and utility of synthesized stable carbenes continues to expand, there is much focus on the tailoring of carbenes to fit specific needs. Several recent reports[11−14] reported the synthesis and theoretical investigations of carbenes with tunable properties. The nucleophilic and electrophilic character of the ambiphilic carbene carbon C2 can be adjusted dramatically through variation of ring size,[13,15] nearby substituents,[16−18] or more delicately by more remote substituent variations.[11,19] Theoretical descriptions of the carbene properties and tuning mechanisms have mostly derived from orbital-based theories and energy decomposition schemes.[13,14,16,20,21] Our previous studies,[22,23] however, have found that orbital based mechanisms are not always recovered by calculations of physical properties with the rigorous quantum theory of atoms in molecules, QTAIM.[24] There are cases though where the QTAIM calculated properties of some NHC−TM complexes do agree with the orbital-based mechanisms.[21,25] Several other studies[4,6] have documented the steric effects of bulky substituents at the ring nitrogen sites that serve to kinetically stabilize the NHC by protecting the carbene carbon from nucleophilic attack. Here we will present a full QTAIM analysis of models of a tunable series of stable carbenes synthesized and characterized recently by Bertrand et al.[11] This study focuses solely on the *electronic* effects of remote substitution at the ring boron sites two bonds removed from the carbene carbon, leaving the steric effects unchanged. The effects of tuning the free NHCs will be measured in the topology of the electron density within the atomic basin of the carbene carbon and in the region of valence shell charge concentration (VSCC) contained therein. The ligand properties will be further analyzed using models of NHC−TM complexes to calculate *trans*-carbonyl stretching frequencies, uncover changes in the QTAIM properties of the NHC, and determine the resultant distribution of charge concentrations and depletions within the TM atomic basin. The latter properties will determine whether the orbital based mechanisms of ligand-to-metal σ-donation and metal-to-ligand π-back-donation are recovered by the QTAIM. Furthermore we will investigate the electronic mechanisms by which variation of the boron substituents causes subtle changes in the ligand properties of the carbene carbon. This includes analysis of the localization and quadrupolar distribution of electron density within atomic basins, the distribution of electron density at bond critical points (BCPs) and interatomic surfaces (IASs), and the delocalization of electrons across atomic basins. These mechanisms will also be verified by the changes in the calculated NMR shielding tensor components of C2. Chemical properties are based on the electron density distribution, which in a stationary state is determined

* Corresponding author. E-mail: d.dupre@louisville.edu.
[†] E-mail: lejohn07@louisville.edu.

10.1021/jp901533g CCC: $40.75
Published on Web 06/23/2009

SCHEME 1

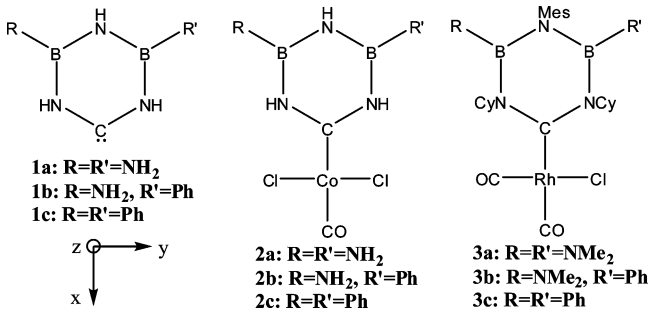

solely through the balance of attractive and repulsive forces acting on the electrons. Physical mechanisms of induction and back-polarization of electron density and their resultant effect on the properties of the carbene carbon will be revealed in the virials of the Ehrenfest forces acting on the electrons integrated over the IASs—the forces that determine changes in the potential energy of bonding interactions.

II. Methods

The equilibrium geometries of the molecules of this study were fully optimized, and normal-mode frequency analysis was performed, using density functional theory (DFT) at B3LYP/6-31G(d,p),[26,27] as implemented in Gaussian03.[28] The coordinates of all optimized models of this study are found in the Supporting Information for this paper.

The resultant electron density, ρ, obtained from the wave function of all optimized structures was analyzed with the quantum theory of atoms in molecules (QTAIM)[24] using the AIM2000 program[29] with wave functions generated with Gaussian03.[28] The atomic overlap matrix (AOM) was obtained by integration of the MO overlap matrix over an atomic basin, and the localization index of atomic basin A, λ(A), and the delocalization index between atoms A and B, δ(A,B), were calculated from the AOM as described by Fradera et al.[30] and Biegler-Konig and Schonbohm.[29] Interatomic surface integrations using AIM2000 yielded the total virial of the force ($V_{(A|B)}$) on the A|B interatomic surface, as well as the virial on the B side of the A|B surface ($V_{B(A|B)}$). Contour plots of the Laplacian of the electron density, $\nabla^2\rho$, and plots of the bond paths (BPs) and interatomic surfaces (IASs) were generated with AIM2000 and refined with graphics software.

Natural bond orbital (NBO)[31] calculations were performed on the optimized structures using NBO 3.1,[32] as implemented in Gaussian03, and NBO 5.0.[31] Second-order perturbation energies, E2, for donor−acceptor orbital interactions were also calculated.

NMR and nucleus-independent chemical shift (NICS)[33] magnetic shielding calculations were performed using the gauge-including atomic orbital (GIAO)[34,35] method at the B3LYP/6-31g(d,p)[26,27] level of theory with Gaussian03.[28] Ghost atoms were placed at 1 Å above the ring critical point (RCP). $NICS_{ZZ}$ values are defined here as the negative of the isotropic magnetic shielding at a distance 1 Å above the ring critical point resulting from a magnetic field applied in the z-direction (see Scheme 1 for direction of coordinates in the molecules of this study).

III. Results and Discussion

1. QTAIM Analysis of the Free NHC Ligands 1a−c. We first looked at the integrated properties, Table 1, of the carbene carbon C2 atomic basin for evidence of tuning of the ligand properties of the NHCs under study. The atomic basin population N(C2) and volume Vol(C2) show essentially no change upon substitution, indicating any changes in ligand properties are due to very subtle electronic effects. The atomic dipole moment μ(C2) increases in magnitude upon amino substitution, and the component of the atomic quadrupole moment tensor corresponding to the "lone pair" direction, Q_{XX}, is most negative for **1a**, with $Q_{XX} = -2.431$ for **1a**, −2.392 for **1b**, and −2.354 for **1c**. More negative quadrupole moments point out directions of higher charge concentration, so this appears to be a clear indicator of the trend in σ-donor ability of these NHCs. This trend, Table 2, is confirmed experimentally by the shifts in the *trans*-carbonyl stretching frequencies in transition metal complexes. In fact, changes in quadrupole moments are often used as evidence of electron delocalization or transfer.[17,36,37]

TABLE 1: Integrated Atomic Properties of the Carbene Carbon C2 in the Free Ligand NHCs 1a−c: Properties of the Electron Density at Critical Points in the Regions of Valence Shell Charge Concentration (VSCC) and Valence Shell Charge Depletion (VSCD)[a]

	1a	1b	1c
C2 Atomic Properties			
N(C2)	5.094	5.095	5.095
Vol(C2)	96.81	96.74	96.94
μ(C2)	1.752	1.743	1.735
Q_{XX}	−2.431	−2.392	−2.354
Q_{YY}	2.824	2.789	2.759
Q_{ZZ}	−0.393	−0.397	−0.405
(3,−3) VSCC CP			
ρ_{VSCC}	0.3322	0.3329	0.3334
$\nabla^2\rho_{VSCC}$	−1.4572	−1.4628	−1.4668
H_{VSCC}	−0.6070	−0.6088	−0.6103
μ_X	−17.0615	−17.1474	−17.2205
μ_Y	−1.0621	−1.0611	−1.0594
μ_Z	−0.9011	−0.9046	−0.9068
α	176	177	177
β	58	58	58
$\rho_{(3,+1)}$VSCD	0.1193	0.1188	0.1185

[a] Atomic basin population N(C2) in e; atomic volume Vol(C2), atomic dipole μ(C2) and quadrupole moments Q_{ii}, VSCC density ρ_{VSCC}, Laplacian $\nabla^2\rho_{VSCC}$, and energy density H_{VSCC}, eigenvalues of the Hessian μ_i, and density of (3,+1) CP of VSCD $\rho_{(3,+1)}$VSCD in au; angles α and β in degrees.

For a more detailed picture, we looked at the properties of ρ at and around the (3,−3) critical point (CP) of the nonbonding valence shell charge concentration (VSCC) at the carbene carbon. Even though ρ_{VSCC} is essentially the same for all three models, the Laplacian $\nabla^2\rho_{VSCC}$ and electronic energy density $H_{VSCC} = V_{VSCC} + K_{VSCC}$ are the most negative for **1c**, Table 1. Thus the VSCC density is more concentrated and tightly held by the nucleus in the atomic basin due to the increased dominance of the attractive potential energy V_{VSCC} over the positive definite electronic kinetic energy K_{VSCC} at the (3,−3) CP. Therefore, **1c** is less prone to serve in σ-donation. The first eigenvalue of the Hessian corresponding to the curvature of ρ in the "lone-pair" direction, μ_X, is also most negative for **1c**, demonstrating that the nonbonding charge is less protruding from the carbene carbon and therefore less poised for nucleophilic attack.

Another aspect of carbene ligand properties is the ability to act as "π-acceptors". A better π-accepting ligand will cause an increase in *trans*-carbonyl stretching frequencies by offsetting the decrease in ν(CO) caused by σ-donation from the ligand to the metal and on to the carbonyl. If we only looked at the component of the quadrupole tensor in the plane-perpendicular direction, Q_{ZZ}, to assess the π-density of the carbene carbon, it

TABLE 2: Calculated Carbonyl Stretching Frequencies and Integrated Atomic Basin and Interatomic Surface Properties of the Carbene Carbon C2 in NHC−TM Complexes 2a−c[a]

	2a	2b	2c
C2 Atomic Properties			
N(C2)	5.031	5.041	5.049
ΔN(C2) [b]	−0.063	−0.054	−0.046
μ(C2)	1.316	1.316	1.312
$\Delta\mu$(C2)[b]	−0.436	−0.427	−0.423
Q_{XX}	−0.573	−0.553	−0.525
ΔQ_{XX}[b]	1.858	1.839	1.829
Q_{ZZ}	−1.891	−1.895	−1.901
ΔQ_{ZZ}[b]	−1.498	−1.498	−1.496
C2−Co Bonding Properties			
R(C2−Co)	1.975	1.973	1.970
ρ_{bcp}(C2−Co)	0.1134	0.1137	0.1141
ρ_{surf}(C2|Co)	0.7675	0.7712	0.7716
C−O Bonding Properties			
ν(CO) calc	2184	2187	2189
ν_{av}(CO) exp[c]	2029	2033	2038
R(C−O)	1.140	1.140	1.140
ρ_{bcp}(C−O)	0.4713	0.4717	0.4721
ρ_{surf}(C|O)	1.6903	1.6907	1.6911
$V_{(C\|O)}$	−1.8400	−1.8405	−1.8409

[a] Atomic basin populations in e; bond lengths R(A−B) in Å; stretching frequencies ν(CO) in cm^{-1}; all other values in au. [b] Changes in QTAIM properties, referenced to models **1**, calculated as $\Delta A = A_2 - A_1$. [c] Reference 11.

would appear that **1a** is the best π-accepting ligand since it has a less negative Q_{ZZ}. We looked further, however, into the details of the valence shell electron density, at both the (3,−3) CP of the VSCC and the (3,+1) CP of the valence shell charge depletion (VSCD) area—the latter region of charge depletion exposes the carbene carbon to nucleophilic attack. This region also leads to the QTAIM analog of orbital-based π-back-bonding. (3,−3) CPs of nonbonding charge concentration on neighboring atoms are found to be polarized toward the VSCD and the exposed carbon nucleus. MacDougall and Bader[38] demonstrated how the contour plot of the Laplacian of ρ in the perpendicular plane of singlet carbenes delineates regions of exposure of C2 to nucleophilic and electrophilic attack. Figure 1 shows the regions of VSCC (black contours protruding outward from the carbon nucleus) and VSCD (green contours above and below the NHC plane). As seen in Table 1, the exposure angle β defined in Figure 1 is the same for all three models, and the density ρ at the (3,+1) CP of the VSCD, $\rho_{(3,+1)}$VSCD, varies only slightly across the series. Furthermore, μ_Z of the (3,−3) VSCC CP, the eigenvalue of the Hessian corresponding to the curvature of electron density in the "π-plane" direction, follows the trend $\mu_Z = -0.9011$ for **1a**, −0.9046 for **1b**, and −0.9068 for **1c**. The more negative μ_Z means the VSCC is most contracted in the z-direction and the zone of VSCD is slightly more diffuse, suggesting that **1c** would actually exhibit better π-accepting character.

2. Properties of the NHC Ligand-TM Complexes 2a−c. While the order of strength of σ-donating ability of the three ligands seems clear on the basis of QTAIM properties, it is not immediately clear which ligand, if any, will be the best π-acceptor. To further understand how the fine-tuning of ligand properties through ring substitution is manifested in QTAIM properties, we performed calculations on corresponding NHC−TM complexes. We used complexes **2a−c** as models of the synthesized[11] NHC−TM complexes **3a−c**, replacing ruthenium with cobalt, a less computationally expensive first-row TM. We also limited the complex to a single carbonyl group in the *trans*-position to separate out calculated stretching frequencies and more easily understand the ligand effects on the electron density. The trends in calculated carbonyl stretching frequencies of the models follow the same trends for the experimental data,[11] suggesting **2a−c** are viable models for the investigation of the ligand properties of the NHCs. The calculated properties of the NHC−TM complexes **2a−c** are presented in Table 2.

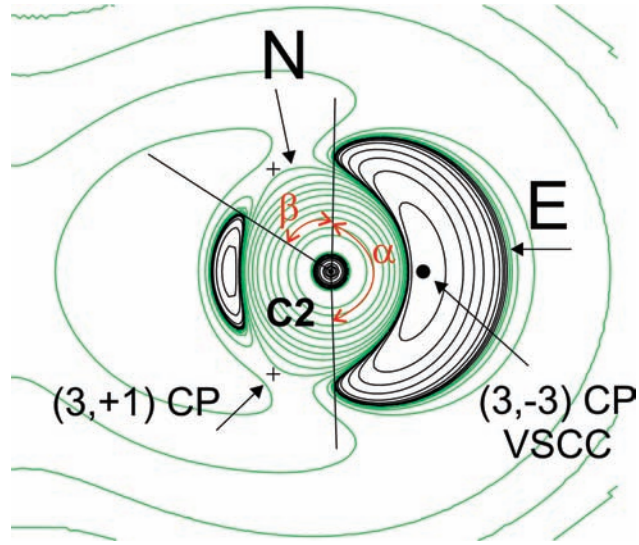

Figure 1. Contour plot of the Laplacian of the electron density in the plane bisecting the ∠N1C2N3 bond angle and perpendicular to the NHC plane in **1a**. Dark contours delineate regions of charge concentration; green lines map regions of charge depletion. The dark circle is the (3,−3) CP of the nonbonding VSCC of C2. The crosses locate two (3,+1) CPs of charge depletion above and below the molecular plane in zones of VSCD (or "holes in the VSCC" as defined by MacDougall and Bader[38]). Two angles are defined as follows: the lone pair extension angle is denoted α, and the valence depletion angle, β. The arrows labeled **N** and **E** show preferred paths of vulnerability to nucleophilic and electrophilic attack.

From an orbital viewpoint, a stronger σ-donating ligand will cause more electron density to be in the antibonding region, σ^*(C−O), of the *trans*-CO, thus weakening the bond and resulting in a decrease in the CO stretching frequency. Conversely, higher π-accepting ability of the NHC ligand leads to more d_π(TM)-to-p_π^*(NHC) back-bonding and a subsequent reduction in the d_π(TM)-to-π^*(*trans*-CO) interaction. This causes a polarization of electron density *away* from the π-antibonding region of the *trans*-CO leading to an increase in CO bond strength and stretching frequency. Because QTAIM calculations deal with properties and resultant forces of the observable real-space electron density, mechanisms derived from orbital-based theories are not always recovered in the QTAIM calculations. Bonding properties are determined by the BCPs and the forces acting on the IASs, and we will look there for the effects of ligand tuning on the TM complexes.

The atomic populations of the carbene carbons in the free ligands **1a−c** are nearly identical (Table 2). The greater σ-donating ability of **1a**, however, leads to a decrease in N(C2) in the TM complex relative to the free ligand, with ΔN(C2) = −0.063 for **2a**, −0.054 for **2b**, and −0.046 for **2c**. This is a significant change where the effects of ligand tuning are clearly seen. The carbene carbon in **2a** also exhibits the largest decrease in the magnitude of μ(C2) and Q_{XX}. The change in the perpendicular atomic quadrupole moment, ΔQ_{ZZ}, however is almost the same for all three models, suggesting there is actually no real difference in the π-accepting abilities of the three free ligands.

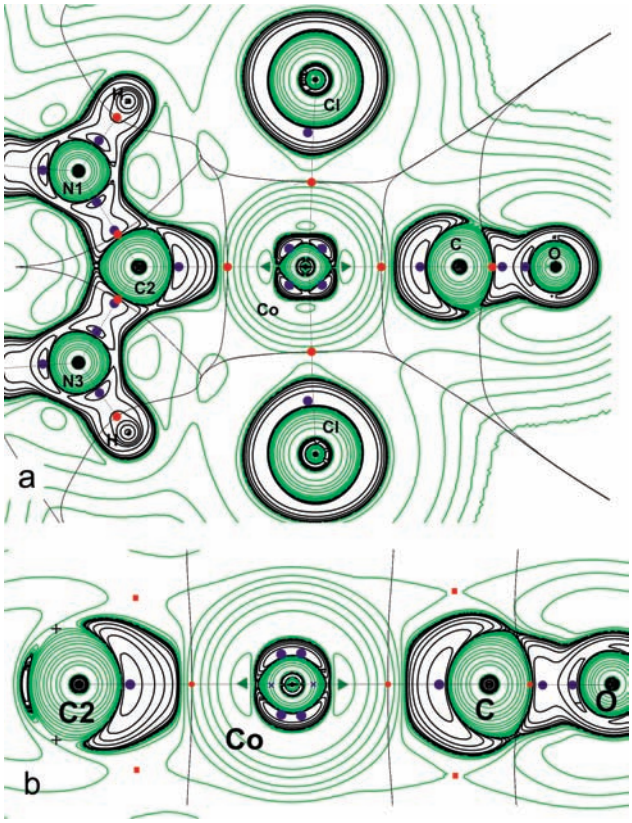

Figure 2. Overlay of BPs (thin dark lines connecting nuclear centers), lines where the IASs (separating the atomic basins) cut the plane of the molecule, BCPs, and contour plot of the Laplacian of the electron density (a) in the plane of the molecule and (b) in the perpendicular plane along the C2−Co−CO axis for **2a**. Red circles denote where BPs and IASs cross at (3,−1) BCPs. Dark circles are bonding or nonbonding (3,−3) CPs of charge concentrations in the valence shells. The ligand bonding (3,−3) CPs of the carbene and carbonyl carbons align with (3,+3) CPs of charge depletion (green triangles) on cobalt. The outer valence shell of Co is diffuse, lying in a region of charge depletion (green contours), while the inner valence shell is condensed into four i-VSCCs in the plane (Figure a) and four more out-of-plane (Figure b). In Figure b, the four out-of-plane i-VSCCs are oriented toward the regions of VSCD of C2 and the carbonyl carbon, with downhill paths leading to (3,−1) saddle points of the Laplacian (red squares) above and below the carbons.

Figures 2a,b illustrate the QTAIM analogs of σ-donation and π-back-donation. The electron density in the outer valence shell of cobalt is very diffuse, and there are no regions of outer-valence shell charge concentration (o-VSCC). This is common for transition metal complexes.[39,40] However, the electron density within the inner valence shell is tightly concentrated and there are (3,−3) CPs of inner-valence shell charge concentrations (i-VSCC). As seen in Figure 2a, the i-VSCC CPs are in an arrangement of maximal ligand avoidance in the plane of ligand coordination, while the (3,−3) CPs of the ligands are aligned with areas of maximal depletion within the i-VSCC of cobalt, as denoted by the (3,+3) CPs about cobalt along the ligand-cobalt BPs. In the plane perpendicular to the ligand plane and passing through C2−Co−CO (Figure 2b), we find four more (3,−3) CPs in the i-VSCC of cobalt. These charge concentrations are polarized toward the regions of VSCD of the carbene and carbonyl carbons, with a downhill gradient path leading to the (3,−1) saddle points of the Laplacian above and below the carbons.

The effects of tuning the ligand properties through substituent variation do not produce significant differences in the QTAIM properties of the C2−Co bonding interaction. The calculated C2−Co bond lengths (Table 2) are in the order **2a** > **2b** > **2c**, and the corresponding electron density values at the BCPs follow the inverse trend but differ only very slightly. Integration over the IAS captures much more of the electron density than the BCP due to the diffuse nature of the bonding between the NHC and TM, but there is still little difference in ρ_{surf}(C2|Co) for the three models, with ρ_{surf}(C2|Co) = 0.7675 for **2a**, 0.7712 for **2b**, and 0.7716 for **2c** (Table 2).

TABLE 3: Bonding Properties for Each Ring Bonding Pair A−B in NHC 1b[a]

atomic basin A	N(A)	λ(A)	V_{surf}(A)	Q_{ZZ}(A)
N1	8.596	7.048	−1.7310	−1.871
N3	8.595	7.037	−1.6856	−1.933
B4	2.832	2.078	−0.7076	−0.844
B6	2.734	2.051	−0.7164	−0.769

bonding pair A−B	δ(A,B)	ρ_{bcp}	$V_{B(A\|B)}$
C2−N1	1.127	0.3091	−0.8833
C2−N3	1.099	0.3050	−0.8342
N1−B6	0.408	0.1899	−0.2254
N3−B4	0.449	0.1929	−0.2177
N5−B6	0.431	0.1967	−0.2468
N5−B4	0.484	0.2009	−0.2402

[a] Integrated atomic populations, N(A), and localization indices, λ(A), in e; atomic surface virial, V_{surf}(A), perpendicular component of atomic quadrupole tensor, Q_{ZZ}(A), delocalization indices, δ(A,B), bond critical point electron density, ρ_{bcp}, and virial of the force on the B-side of the A|B IAS, $V_{B(A|B))}$, all in au.

Likewise, despite differences of 2−3 wavenumbers in the *trans*-carbonyl stretching frequencies, the changes in the *trans*-carbonyl CO bonding properties obtained from QTAIM calculations are very subtle. ν(CO) is highest for **2c** (and experimentally[11] for **3c**), so the calculated properties should indicate a stronger bonding interaction. The calculated bond lengths, however, are the same for all three models, with R(C−O) = 1.140 Å. The electron density at the BCP increases only 0.0008 au across the series, with ρ_{bcp}(C−O) = 0.4713 for **2a**, 0.4717 for **2b**, and 0.4721 for **2c**. The same variance is seen in integrating the electron density over the entire IAS, ρ_{surf}(C|O). The virial of the Ehrenfest forces acting on the IAS, $V_{(A|B)}$, is a measure of the stabilizing potential energy density due to surface formation. Greater attractive forces at the C|O surface lead to a stabilization of the IAS in **2b** over **2a** by 0.0005 hartree—or 0.3 kcal/mol—with approximately the same increase in **2c** over **2b**.

3. Mechanism of the Electronic Tuning of Ligand Properties. To examine the electronic mechanisms involved in the tuning of ligand properties through variation of the ring substituents, it is most convenient to consider model **1b** as it contains both the amino and phenyl substituents. All of the trends in **1b** translate to the comparison of the other models. Table 3 contains the integrated atomic properties of N1, B6, N3, and B4 (atom numbering shown in Scheme 2). For each bonding pair A−B in model **1b**, Table 3 lists the bond critical point densities ρ_{bcp}, delocalization indices, and the virial of the force on the B-side of the A|B IAS. Effects of amino substitution are seen on the C2−N1−B6−N5 side of the ring, phenyl substitution on the C2−N3−B4−N5 side.

As expected, the integrated atomic population of B6, N(B6) = 2.734, is less than that of B4, N(B4) = 2.832, due to the inductive effect of the amino nitrogen. Präsang et al.[11] state that the σ-donor ability of the NHC ligands decreases "following the donor ability of the boron substituents." Our previous

SCHEME 2: Atom Numbering for Model 1b, Hydrogens Removed

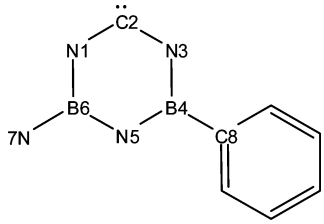

theoretical studies,[22,23] however, have shown substituted amino groups to cause electronic changes through mechanisms of induction and subsequent back-polarization,[38] rather than π-back-donation. Indeed, with models **1a** and **1b**, there are (3,−3) CPs above and below the exo amino nitrogens N_{exo}, indicating the presence of localized nonbonding lone-pair-like charge concentrations. Loss of those nonbonding charge concentrations would have indicated back-donation of π-density to the ring borons.[38] The charge concentrations are, however, tilted toward the electron deficient borons but are well contained within the nitrogen atomic basins, as seen in Figure 3. In **1b**, the perpendicular component of the quadrupole moment is actually *less negative* for Q_{ZZ}(B6) = −0.769 (with the amino substituent) than for Q_{ZZ}(B4) = −0.844 (with the phenyl substituent). This does not seem to indicate π-back-donation from the more electronegative amino nitrogen into the atomic basin of the electropositive boron. Likewise there is less π-plane distribution of electron density in the adjacent ring nitrogen, with Q_{ZZ}(N1) = −1.871 and Q_{ZZ}(N3) = −1.933. The NICS gauge of aromaticity even indicates *less* aromatic delocalization upon amino substitution, with $NICS_{ZZ}$ = −4.23 for **1c**, −2.56 for **1b**, and −1.45 for **1a**.

With the withdrawal of electron density away from boron by the amino nitrogen, there is greater electron density concentrated at the B−N_{exo} BCP. In **1b**, ρ_{bcp}(B6−N7) = 0.2014 as compared to ρ_{bcp}(B4−C8) = 0.1849. The higher density at the B6−N7 BCP causes subsequent electrostatic back-polarization of the remaining B6 electron density in the direction of the ring nitrogens N1 and N5 along the bond paths. The B6−N1 bonding electron density is less shared and more localized within the nitrogen atomic basin, where λ(N1) = 7.048 as compared to λ(N3) = 7.037. Conversely, the delocalization between B4 and the ring nitrogens N3 and N5 is much higher because of the less electronegative R-group. On the phenyl side of the ring in **1b**, δ(N3,B4) = 0.449 and δ(N5,B4) = 0.484, versus the amino side of the ring where δ(N1,B6) = 0.408 and δ(N5,B6) = 0.431, indicating less electron sharing in the latter bonds.

With δ(N1,B6) lower than δ(N3,B4), there is a subsequent higher electron delocalization between N1 and C2; δ(C2,N1) = 1.127, whereas on the phenyl side of the ring, δ(C2,N3) = 1.099. The higher C2−N1 delocalization and higher electron density at the C2−N1 BCP, where ρ_{bcp}(C2−N1) = 0.3091 and ρ_{bcp}(C2−N3) = 0.3050 produces a larger back-polarization of the nonbonding C2 VSCC outward from the NHC ring. These changes in the polarization and delocalization of electrons around the ring, caused by the R-group substitution of phenyl for amino, lead to the changes in the ligand properties described above. It is the electron withdrawal by the amino group and the subsequent back-polarization of ring charge that causes **1a** to be the best σ-donor ligand of the three models.

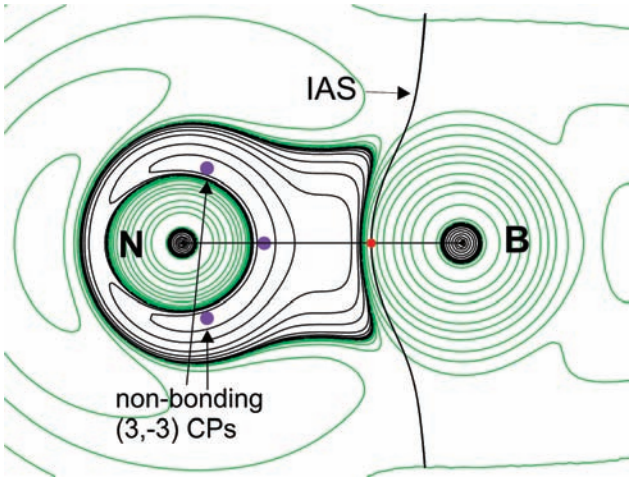

Figure 3. Overlay of BP connecting boron and nitrogen nuclear centers, line where B|N IAS cuts the plane of the plot, and contours of the Laplacian of the electron density in the plane perpendicular to the NHC molecular plane and passing through the B−N_{exo} bond axis for **1a**. Blue circles are (3,−3) CPs of VSCC, and the red circle is the B−N BCP. Nonbonded charge concentrations are tilted toward the severely depleted boron atomic basin but are still concentrated within the more electronegative nitrogen atomic basin. The back-polarization effect on the IAS is similar to that seen in Figure 5 of ref 38.

TABLE 4: Isotropic Shielding Tensor Components (in ppm) of C2 with Calculated and Experimental ^{13}C Chemical Shifts for NHCs 1a−c[a]

tensor component	1a	1b	1c
σ_{xx}	−15.81	−16.17	−16.46
σ_{yy}	−388.24	−403.19	−417.00
σ_{zz}	156.02	156.41	157.21
σ_{iso}	−82.68	−87.65	−92.09
calculated shift, δ	274.48	279.45	283.89
experimental shift[c]	282.9	281.5	281.6

[a] See Scheme 1 for definition of axes. [b] $\delta = \sigma(TMS) - \sigma_{iso}$, where σ(TMS) = 191.8 ppm. [c] See ref 11.

These mechanisms and the changes in the outward-polarization of the C2 VSCC are recovered in the calculated C2 magnetic shielding tensors listed in Table 4. In singlet carbenes, the isotropic shielding of the carbon nucleus is dominated[41] by the *y*-component of the paramagnetic term, σ_{yy}, as illustrated by the Ramsey formalism,[42] eq 1.

$$\sigma_{yy}^{p} = -\frac{e^2\mu_\circ}{4\pi m_e^2}\sum_n \frac{\langle 0|l_y|n\rangle}{E_\circ - E_n}\left\langle n\left|\frac{l_y}{r^3}\right|0\right\rangle \qquad (1)$$

In a *y*-applied magnetic field, the angular momentum operator l_y rotates the nonbonding charge concentration into the region of charge depletion, thus leading to strong deshielding currents. The paramagnetic term is especially sensitive[41] to changes in the electron density distribution as it depends on $1/r^3$, where r is the distance between the electron and the nucleus. Therefore, the more diffuse nonbonding VSCC in **1a** leads to a less deshielding σ_{yy} component of −388.24 ppm. Conversely, the VSCC is less polarized and more tightly concentrated at the (3,−3) CP of the VSCC in **1c**, as seen by the greater magnitude of ρ_{VSCC} and $\nabla^2\rho_{VSCC}$ and the less-negative quadrupole tensor component Q_{XX} in Table 1. With more electron density concentrated closer to the C2 nucleus, the σ_{yy} shielding tensor component is more deshielding, with σ_{yy} = −417.00 ppm in **1c**.

Changes in the virial of the Ehrenfest force acting on the interatomic surfaces provide further evidence of the increased

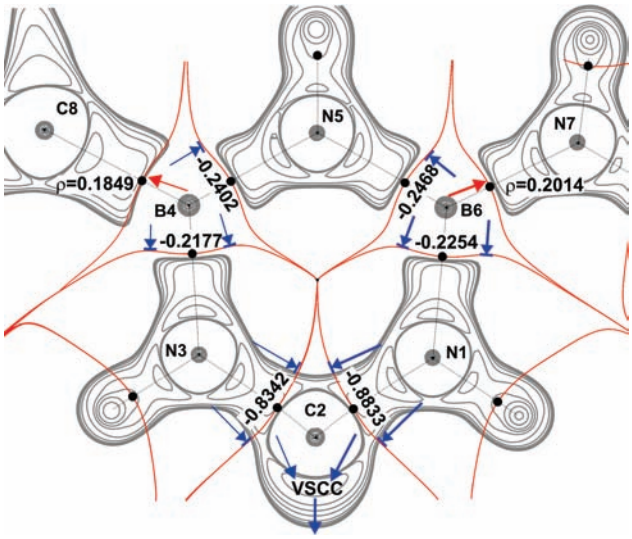

Figure 4. Representation of the increase in the induction/back-polarization mechanism due to amino substitution in **1b.** Overlay of BPs (thin dark lines connecting nuclear centers), lines (red) where the IASs cut the plane of the molecule, and contours of the Laplacian of the electron density corresponding only to charge concentrations in the plane of the NHC **1b**. Depletion contours omitted for clarity. Blue arrows at IASs denote the virial of the force acting on that side of the IAS, with selected values given. Inductive withdrawal of electron density from boron by the R groups is indicated by red arrows, with corresponding values of ρ at the B6−N7 and B4−C8 BCPs given. Resultant outward polarization of C2 VSCC and increased σ-donation ability is indicated by blue arrows within the C2 atomic basin.

back-polarization of density around the ring with amino substitution. An increase in the virial of the force on the B-side of an A|B IAS, $V_{B(A|B)}$, can be due to an increased attraction of the B electrons by A *or* by a force pushing the B electrons toward A. Again, when the amino- and phenyl-substituted sides of the NHC **1b** are compared, the induction by the amino nitrogen and subsequent back-polarization causes increased pressure of the electron density against the boron side of the B6|N1 and B6|N5 interatomic surfaces. The virial of the force on the B6 side of the B6|N1 and B6|N5 surfaces in **1b** is −0.2254 and −0.2468 au, respectively. On the phenyl side, with less induction/back-polarization, $V_{B4(N3|B4)} = V0.2177$ and $V_{B4(N5|B4)} = -0.2402$ au. There is subsequently a greater virial of force $V_{N1(C2|N1)} = -0.8833$ au on the N1 side of the N1|C2 IAS, compared to $\nabla_{N3(C2|N3)} = -0.8342$ au.

Figure 4 represents the inductive withdrawal (red arrows) and subsequent back-polarization of charge (blue arrows) in the NHC **1b**. The darker blue arrows on the amino-substituted side of the NHC ring indicate the increased pressure on the IASs, with the corresponding surface virial values given. These long-range polarization effects redound on the outward polarization of the nonbonding VSCC of C2, represented by the blue arrows within the C2 atomic basin in Figure 4. This results in the ordering of σ-donor ligand strength **1a** > **1b** > **1c**. At the suggestion of one of the reviewers, we have performed similar calculations with a hypothetical R = R′ = NO_2 substitution on the NHC **1** and NHC−TM complex **2**. As expected, we find this produces trends opposite to that obtained when R = NH_2. Since the oxygen atoms reduce the electronic population in the atomic basins of the exo nitrogens, withdrawal of electron density out of the ring is reduced. Subsequently, there is much less back-polarization into the ring. The net result is greater, more uniform electron delocalization throughout the ring, and the nonbonding VSCC of C2 is not nearly as polarized—it is more concentrated and tightly held near the VSCC CP. As a result, this NHC is predicted to be a very weak σ-donor and π-acceptor. Indeed, the calculated *trans*-carbonyl stretching frequency is 17 cm^{-1} higher than in **2c**. We find that the substitution with R = NO_2 produces effects that go beyond the intent and theme of this paper which is meant to deal with subtle, fine-tuning of the reactive properties of the carbene carbon in molecules for which there is experimental data for corroboration with theory. The details of our calculations involving the nitro group are found in the Supporting Information for this paper.

IV. Conclusions

The full QTAIM analysis of NHCs **1a**−**c** reported here recovers the experimentally observed tuning of the strength of ligand-to-metal σ-donation. Amino substitution at the ring borons in **1a** and **1b** leads to increased outward distribution of the nonbonding VSCC at the carbene carbon C2. This is evident in the integrated atomic dipole and quadrupole moments, μ(C2) and Q_{XX}(C2), and by the reduced radial curvature of the VSCC in **1a**, determined by μ_X. The greater outward polarization of the C2 VSCC in **1a** leads to a larger loss of integrated atomic charge N(C2) upon formation of the TM complex **2a**, as compared to **1b** with one amino substituent, and **1c** with none. This tuning of σ-donating ability is also apparent from the changes in μ(C2) and Q_{XX}(C2) when the NHC−TM complexes **2a**−**c** are formed. From the QTAIM perspective, the remote amino substitution on the NHC causes a subtle destabilization of the C|O IAS and a lowering of the virial of force, $V_{(C|O)}$, acting on that surface. The resultant effect is seen both experimentally and theoretically by the decrease in the stretching frequency of the *trans*-carbonyl group, with ν(CO) of **2a** < **2b** < **2c**.

As was found in our previous studies, the orbital-based mechanisms of the effects of amino substitution are not recovered by QTAIM calculations. There is no evidence of back-donation of π-electron density from the exo nitrogen to boron and the NHC ring. In fact, the (3,−3) nonbonding CPs of the exo nitrogens are tilted toward the NHC but well contained within the N_{exo} atomic basins. Rather it is the inductive withdrawal of charge by the exo nitrogen and the subsequent electrostatic back-polarization of the remaining boron electron density that produces ligand tuning effects. Back-polarization results in an increase in the virial of the Ehrenfest force acting on the boron side of the $B|N_{ring}$ IASs. This in turn increases the outward polarization of the C2 VSCC and the σ-donating ability of the NHC ligand.

Acknowledgment. Supercomputer time allocations received from the University of Kentucky High Performance Computing Complex and from the Advanced Biomedical Computing Center of the Frederick Cancer Research and Development Center, National Institutes of Health, are acknowledged. Support for this work also came from a Research Initiation Grant from the Office of the Vice President for Research, University of Louisville, and an Intramural Research Grant from the College of Arts and Sciences, University of Louisville.

Supporting Information Available: Complete author list for ref 28. Tables S1−S3 with calculated atomic properties, stretching frequencies, and bonding properties for the NO_2 substituted models **1-NO₂** and **2-NO₂**. This material is available free of charge via the Internet at http://pubs.acs.org.

References and Notes

(1) (a) Öfele, K. *J. Organomet. Chem.* **1968**, *12*, P42−P43. (b) Wanzlick, H.-W.; Schönherr, W. *Angew. Chem., Int. Ed.* **1968**, *7*, 141–142.

(2) Arduengo, A. J., III.; Harlow, R. L.; Kline, M. *J. Am. Chem. Soc.* **1991**, *113*, 361–363.

(3) Herrmann, W. A. *Angew. Chem., Int. Ed.* **2002**, *41*, 1290–1309.

(4) Díez-González, S.; Nolan, S. P. *Coord. Chem. Rev.* **2007**, *251*, 874–883.

(5) Crudden, C. M.; Allen, D. P. *Coord. Chem. Rev.* **2004**, *248*, 2247–2273.

(6) Cavallo, L.; Correa, A.; Costabile, C.; Jacobsen, H. *J. Organomet. Chem.* **2005**, *690*, 5407–5413.

(7) Alder, R. W.; Blake, M. E.; Chaker, L.; Harvey, J. N.; Paolini, F.; Schutz, J. *Angew. Chem., Int. Ed.* **2004**, *43*, 5896–5911.

(8) Nair, V.; Bindu, S.; Sreekumar, V. *Angew. Chem., Int. Ed.* **2004**, *43*, 5130–5135.

(9) (a) Perry, M. C.; Burgess, K. *Tetrahedron Asym.* **2003**, *14*, 951–961. (b) Enders, D.; Gielen, H. *J. Organomet. Chem.* **2001**, *617*−*618*, 70–80.

(10) Frey, G. D.; Lavallo, V.; Donnadieu, B.; Schoeller, W. W.; Bertrand, G. *Science* **2007**, *316*, 439–441.

(11) Präsang, C.; Donnadieu, B.; Bertrand, G. *J. Am. Chem. Soc.* **2005**, *127*, 10182–10183.

(12) Schoeller, W. W.; Frey, G. D.; Bertrand, G. *Chem.*−*Eur. J.* **2008**, *14*, 4711–4718.

(13) Kausamo, A.; Tuononen, H. M.; Krahulic, K. E.; Roesler, R. *Inorg. Chem.* **2008**, *47*, 1145–1154.

(14) Jacobsen, H.; Correa, A.; Costabile, C.; Cavallo, L. *J. Organomet. Chem.* **2006**, *691*, 4350–4358.

(15) Ishida, Y.; Donnadieu, B.; Bertrand, G. *Proc. Natl. Acad. Sci. U.S.A.* **2006**, *103*, 13585–13588.

(16) Schoeller, W. W.; Eisner, D.; Grigoleit, S.; Rozhenko, A. B.; Alijah, A. *J. Am. Chem. Soc.* **2000**, *122*, 10115–10120.

(17) Tafipolsky, M.; Scherer, W.; Ofele, K.; Artus, G.; Pedersen, B.; Herrmann, W. A.; McGrady, G. S. *J. Am. Chem. Soc.* **2002**, *124*, 5865–5880.

(18) Lavallo, V.; Canac, Y.; Präsang, C.; Donnadieu, B.; Bertrand, G. *Angew. Chem., Int. Ed.* **2005**, *44*, 5705–5709.

(19) Leuthäu*β*er, S.; Schwarz, D.; Plenio, H. *Chem.*−*Eur. J.* **2007**, *13*, 7195–7203.

(20) Jacobsen, H.; Correa, A.; Poater, A.; Costabile, C.; Cavallo, L. *Coord. Chem. Rev.* **2009**, *253*, 687–703.

(21) Frenking, G.; Solà, M.; Vyboishchikov, S. F. *J. Organomet. Chem.* **2005**, *690*, 6178–6204.

(22) Johnson, L. E.; DuPré, D. B. *J. Phys. Chem. A* **2007**, *111*, 11066–11073.

(23) Johnson, L. E.; DuPré, D. B. *J. Phys. Chem. A* **2008**, *112*, 7448–7454.

(24) (a) Bader, R. F. W. *Atoms in molecules. A quantum theory*; Clarendon Press: Oxford, U.K., 1990. (b) Bader, R. F. W.; Fang, D.-C. *J. Chem. Theory. Comput.* **2005**, *1*, 403–414. (c) Bader, R. F. W. *Int. J. Quantum Chem.* **2003**, *94*, 173–177.

(25) Poater, J.; Cases, M.; Fradera, X.; Duran, M.; Solà, M. *Chem. Phys.* **2003**, *294*, 129–139.

(26) Becke, A. D. *J. Chem. Phys.* **1993**, *98*, 5648–5652.

(27) Lee, C.; Yang, W.; Parr, R. G. *Phys. Rev.* **1988**, *B37*, 785–789.

(28) Frisch, M. J.; et al. *Gaussian03*, revision E.01; Gaussian, Inc.: Wallingford, CT, 2004.

(29) Biegler-Konig, F.; Schonbohm, J. *J. Comput. Chem.* **2002**, *23*, 1489–1494.

(30) Fradera, X.; Austen, M. A.; Bader, R. F. W. *J. Phys. Chem. A.* **1999**, *103*, 304–314.

(31) Glendening, E. D.; Badenhoop, J. K.; Reed, A. E.; Carpenter, J. E.; Bohmann, J. A.; Morales, C. M.; Weinhold, F. *NBO 5.0 Program Manual. Natural Bond Orbital Analysis Programs, NBO 5.0*; Theoretical Chemistry Institute, University of Wisconsin: Madison, WI, 2001.

(32) Glendening, E. D.; Reed, A. E.; Carpenter, J. E.; Weinhold, F. *NBO Version 3.1 Program Manual*. Theoretical Chemistry Institute and Department of Chemistry: University of Wisconsin: Madison, WI, 1990.

(33) Chen, Z.; Wannere, C. S.; Corminboeuf, C.; Puchta, R.; Schleyer, P. v. R. *Chem. Rev.* **2005**, *105*, 3842–3888, and references therein.

(34) Ditchfield, R. *Mol. Phys.* **1974**, *27*, 789–807.

(35) Wolinksi, K.; Hinton, J. F.; Pulay, P. *J. Am. Chem. Soc.* **1990**, *112*, 8251–8260.

(36) Vidal, I.; Melchor, S.; Dobado, J. A. *J. Phys. Chem. A* **2005**, *109*, 7500–7508.

(37) Cortés-Guzmán, F.; Bader, R. F. W. *Coord. Chem. Rev.* **2005**, *249*, 633–662.

(38) MacDougall, P. J.; Bader, R. F. W. *Can. J. Chem.* **1986**, *64*, 1496–1508.

(39) MacDougall, P. J.; Hall, M. B. *Trans. Am. Cryst. Assoc.* **1993**, *26*, 105–123.

(40) MacDougall, P. J.; Hall, M. B.; Bader, R. F. W.; Cheeseman, J. R. *Can. J. Chem.* **1989**, *67*, 1842–1846.

(41) Wiberg, K. B.; Hammer, J. D.; Keith, T. A.; Zilm, K. *J. Phys. Chem. A* **1999**, *103*, 21–27.

(42) Ramsey, N. F. *Phys. Rev.* **1950**, *78*, 699.

JP901533G